HiZELS: a high redshift survey of Hα emitters. I: the cosmic star-formation rate and clustering at z = 2.23[⋆]

J. E. Geach[1]†, Ian Smail[1], P. N. Best[2], J. Kurk[3], M. Casali[4], R. J. Ivison[2,5] & K. Coppin[1]

[1]*Institute for Computational Cosmology, Durham University, South Road, Durham. DH1 3LE. UK.*

[2]*SUPA, Institute for Astronomy, Royal Observatory, University of Edinburgh, Blackford Hill, Edinburgh. EH9 3HJ. UK.*

[3]*Max-Planck-Institut für Astronomie, Königstuhl, 17 D–69117, Heidelberg, Germany*

[4]*European Southern Observatory, Karl-Schwarzschild-Strasse 2, D–85738 Garching, Germany*

[5]*Astronomy Technology Centre, Royal Observatory, University of Edinburgh, Blackford Hill, Edinburgh. EH9 3HJ. UK.*

ABSTRACT

We present results from a near-infrared narrow-band survey of emission-line galaxies at $z = 2.23$, using the Wide Field Camera on the United Kingdom Infrared Telescope. The H_2S1 narrow-band filter ($\lambda_c = 2.121\mu$m) we employ selects the Hα emission line redshifted to $z = 2.23$, and is thus suitable for selecting 'typical' star forming galaxies and active galactic nuclei at this epoch. The pilot study was undertaken in the well studied Cosmological Evolution Survey field (COSMOS) and is already the largest near-infrared narrow-band survey at this depth, with a line flux limit of $F_{H\alpha} \sim 10^{-16}$ erg s^{-1} cm^{-2} over 0.60 square degrees, probing $\sim 220 \times 10^3$ Mpc^3 (co-moving) down to a limiting star formation rate of $\sim 30\, M_\odot$ yr^{-1} (3σ). In this paper we present the results from our pilot survey and evaluate the Hα luminosity function and estimate the clustering properties of Hα emitters at $z = 2.23$ from 55 detected galaxies. The integrated luminosity function is used to estimate the volume averaged star formation rate at $z = 2.23$: $\rho_{SFR} = 0.17^{+0.16}_{-0.09}\, M_\odot$ yr^{-1} Mpc^{-3} for $L_{H\alpha} > 10^{42}$ erg s^{-1}. For the first time, we use the Hα star-formation tracer to reliably constrain ρ_{SFR} out to $z = 2.23$ demonstrating the rapid increase in ρ_{SFR} out to this redshift as well as confirming the flattening in ρ_{SFR} between $z \sim 1$–2. In addition to the luminosity distribution, we analyse the clustering properties of these galaxies. Using the 2-point angular correlation function, $\omega(\theta)$, we estimate a real space correlation length of $r_0 = 4.2^{+0.4}_{-0.2}\, h^{-1}$ Mpc. In comparison to models of clustering which take into account bias evolution, we estimate that these galaxies are hosted by dark matter halos of mass $M_{halo} \sim 10^{12}\, M_\odot$ consistent with the progenitors of the Milky Way.

Key words: galaxies: high-redshift, luminosity function, evolution, cosmology: observations

1 INTRODUCTION

One of the most fundamental, and challenging, goals of modern observational cosmology is to reliably determine the volume-averaged star-formation history of the Universe: its distribution function and variation with environment are powerful tools for understanding the physics of galaxy formation and evolution. Surveys using a range of star-formation indicators suggest that the star-formation rate density (ρ_{SFR}) rises as $\sim (1 + z)^4$ out to $z \sim 1$ (e.g. Lilly et al. 1995) and hence the 'epoch' of galaxy formation must occur at $z > 1$. Unfortunately, tying down the precise epoch of maximum activity at $z > 1$ is more difficult, with different star-formation indicators giving a wide spread in ρ_{SFR} (e.g. Smail et al.

2002; Hopkins 2004) – although there is a general trend for ρ_{SFR} to plateau at $z \sim 2$ and hence it is likely that many of the stars seen in galaxies at the present-day were formed between $z \sim 1$–3. Indeed, $z \sim 2$–2.5 appears to be a critical era in the evolution of many populations: optical QSO activity (which should be linked to the growth of super-massive black holes) peaks at this epoch (Boyle et al. 2000), as does the luminosity density in bright submillimetre galaxies – thought to represent an early phase in the formation of massive galaxies (Chapman et al. 2005). This behaviour might be associated with the formation of spheroids or the most massive galaxies. It is not clear that this evolution is true of "typical" star forming galaxies (i.e. those with SFRs $<100\, M_\odot$ yr^{-1}). A sensitive survey of star forming galaxies in a range of representative environments at high-z is needed to address this issue.

Variation between the different ρ_{SFR} measurements at high-z is in part due to a combination of the effects of sample selection, Cosmic variance and biases in individual indicators. Estimates

from ultra-violet–selected samples (e.g. Madau et al. 1996) require large corrections for dust extinction and may miss the most obscured sources altogether. Similarly, although far-infrared-selected samples are less influenced by dust extinction, they require large extrapolations to account for sources below their bright luminosity limits (e.g. Chapman et al. 2005). Thus while no single indicator can give an unbiased view of the evolution of the ρ_{SFR}, mixing different indicators at different epochs is not helping our understanding.

What we require is one star-formation indicator that can be applied from $z = 0$–3, is relatively immune to dust extinction and which has sufficient sensitivity that ρ_{SFR} estimates do not require large extrapolations for faint sources. The Hα emission line luminosity is a well-calibrated SFR indicator providing a good measure of the instantaneous SFR of young, massive stars ($>8\,M_\odot$; Kennicutt 1998). Thus Hα combines all of these properties and hence is the tool of choice for studying the evolution of the SFR density out to $z \sim 3$ – covering the expected peak in the SFRD. The Hα luminosity function (LF), and the corresponding ρ_{SFR} has been measured out to to $z \sim 1.3$ by a series of investigators (e.g. Gallego et al. 1995; Tresse et al. 2002; Yan et al. 1999; Shioya et al. 2008; Villar et al. 2008). These observations confirm the rapid rise seen by other indicators out to $z \sim 1$ (see also the compilation of Moorwood 2004).

At higher redshift attempts to search for Hα emission have been made with near-infrared narrow-band surveys (e.g. Thompson et al. 1996; Moorwood et al. 2000), but these have been hampered by small survey areas. At the typical limit of these studies, $F_{\mathrm{H}\alpha} \sim 10^{-16}\,\mathrm{erg\,s^{-1}\,cm^{-2}}$, only a handful of potential $z \sim 2$ Hα emitters have been detected. Indeed, in the largest survey of this type to date, Thompson et al. (1996) detected only *one* Hα emitter over 276 square arcminutes to a flux limit of $F_{\mathrm{H}\alpha} = 3.5 \times 10^{-16}\,\mathrm{erg\,s^{-1}\,cm^{-2}}$. This was confirmed to have an emission line corresponding to $z = 2.43$ in the follow-up spectroscopic survey of Beckwith et al. (1998). In comparison, Moorwood et al. (2000) probe to a slightly deeper limit, $F_{\mathrm{H}\alpha} = 0.5 \times 10^{-16}\,\mathrm{erg\,s^{-1}\,cm^{-2}}$ over 100 square arcminutes, and detect 10 candidate emitters, but all of the candidates chosen for spectroscopic follow-up turned out to be higher redshift [OIII]λ5007 emitters (Kurk et al. 2004; Moorwood et al. 2003). Detecting large numbers of Hα emitters using this method is clearly challenging, and larger (and preferably deeper) surveys are needed to efficiently probe the Hα luminosity density at high redshift.

Larger scale narrow-band imaging surveys would also present the opportunity to measure the clustering properties of high-z star forming galaxy populations. Not only does this provide an important insight into the real space distribution of galaxies, but (assuming a model for bias – i.e. how the observed galaxy populations trace the underlying matter distribution) can provide an estimate of the mass of dark matter halos that host such galaxies. Comparing the measurements of clustering for populations at high and low redshift, it is therefore possible to infer the likely progenitor populations of galaxies seen in the local Universe.

In this paper we make an improvement over previous $z \sim 2$ Hα surveys by utilising the panoramic imaging capability of the Wide Field Camera (WFCAM, Casali et al. 2007) on the 3.8-m United Kingdom Infrared Telescope (UKIRT). We have obtained deep narrow-band imaging at $\lambda = 2.121\,\mu$m to search for $z = 2.23$ Hα emitters over 0.603 sq. degrees of the Cosmological Evolution Survey field (COSMOS) (Scoville et al. 2007). This corresponds to a co-moving volume $\sim 30\times$ that probed by Moorwood et al. (2000), which is the most similar previous survey in redshift cover-

age and depth to this one. Here we present the results of our pilot survey, and use the Hα LF to evaluate the Hα luminosity density at $z = 2.23$, and hence constrain the evolution of ρ_{SFR}. In §2 we outline the details of the survey and reduction techniques, §3 describes the narrow-band selection procedure, and in §4 we present the results, discuss some of the individual properties and calculate the luminosity function for the Hα sample. We compare our results with previous estimates for this epoch, and with the latest semi-analytic predictions for the Hα luminosity density at this epoch. The integrated luminosity function provides us with the ρ_{SFR}, and we compare this to other measurements to place our result in a cosmological context. We also present the first clustering analysis of Hα emitters at high redshift. The two-point angular correlation function yields the real-space correlation length, which we compare to other populations over cosmic time to gain insight into the likely descendants of these galaxies. We summarise the work in §5 and give a brief overview of our future extension to the survey. Throughout we have assumed $h = 0.7$ in units of $100\,\mathrm{km\,s^{-1}\,Mpc^{-1}}$ and $(\Omega_m, \Omega_\Lambda) = (0.3, 0.7)$. Unless otherwise stated, all magnitudes are on the Vega scale.

## 2 OBSERVATIONS AND DATA REDUCTION

2.1 Observations

The COSMOS field was observed during 2006 May, November and December with WFCAM on UKIRT, with the broadband (K-band) and narrow-band (H$_2$S1, $\lambda_c = 2.121\,\mu$m, $\delta\lambda = 0.021\,\mu$m) filters. WFCAM's standard 'paw-print' configuration of four 2048$\times$2048 0.4$''$/pixel detectors offset by $\sim$20$'$ can be macro-stepped four times to mosaic a contiguous region of $\sim$55$'$ $\times$ 55$'$ (Casali et al. 2007). In this way we mapped 3 paw-prints, or $\sim$0.62 square degrees of COSMOS (centred on $10^{\mathrm{h}}00^{\mathrm{m}}28.6^{\mathrm{s}}$, $+02^{\mathrm{d}}12'21.0''$ J2000). Our narrow-band exposure time is $\sim$13.5 ks/pixel (in order to reach the equivalent continuum limit, the broad-band K exposures were $\sim$0.5 ks/pixel). The seeing was consistently of the order $\lesssim$1$''$. To help with Cosmic ray rejection over the relatively long narrow-band exposures (40 or 60 s), we used the NDR (Non Destructive Read) mode, whereas CDS (Correlated Double Sampling) mode was used for the broad-band exposures. The near-infrared observations were obtained in the standard way, following a 14-point jitter pattern. In addition to the jitter pattern, to improve sampling of the PSF with the 0.4$''$ pixels of WFCAM, the narrow-band frames were microstepped in a 2 $\times$ 2 grid with 1.2$''$ offsets at each position. We summarise the observations in Table 1.

2.2 WFCAM data reduction

For a given frame in a jitter sequence of 14 images, we self-flat the data using a normalised median combination of the remaining frames in the sequence, taking care to mask-out bright objects in each frame. This is achieved by creating a two-pass flat: in the first pass a rough flat field image is made from a straight median combination of the data frames in order to reveal the bright objects. In the next step, we use SEXTRACTOR's check_image output (v2.3.2 Bertin & Arnouts 1996) to identify regions where bright stars and galaxies lie and then mask these when constructing the master flat. This minimises the artifacts seen around bright sources. Some care must be taken with the micro-stepped frames – the small offset between consecutive frames in a micro-sequence are smaller

Table 1. Observation log of the COSMOS field. Coordinates are in J2000 and refer to the centre pointing of a WFCAM 'paw-print'. The average seeing in the broad and narrow-band frames (stacked frames) is $\sim 1''$.

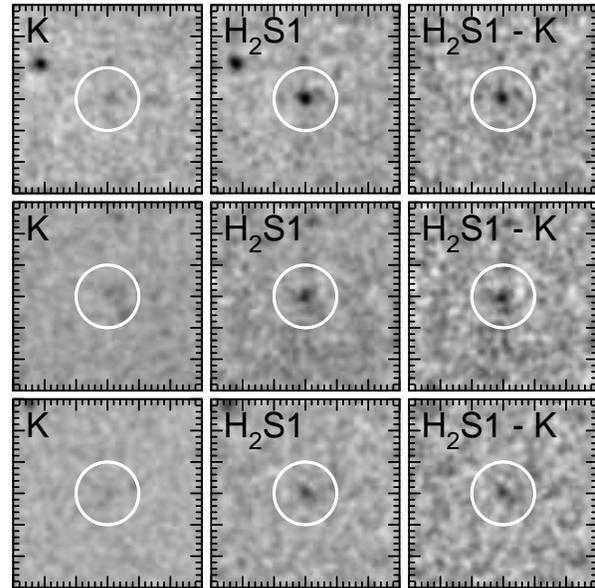| Field I.D.	R.A. (h m s)	Dec. (° ′ ″)	Dates observed	H$_2$S1 exposure time (ksec.)	Continuum (K) depth (3σ mag)
COSMOS 2	10 00 52	+02 10 30	20–26 May / 5, 14–20 December 2006	15.9	20.1
COSMOS 3	10 00 00	+02 23 44	20–26 May / 5, 14–20 December 2006	13.4	20.0
COSMOS 4	10 00 53	+02 23 44	13–17 November 2006	13.6	20.1
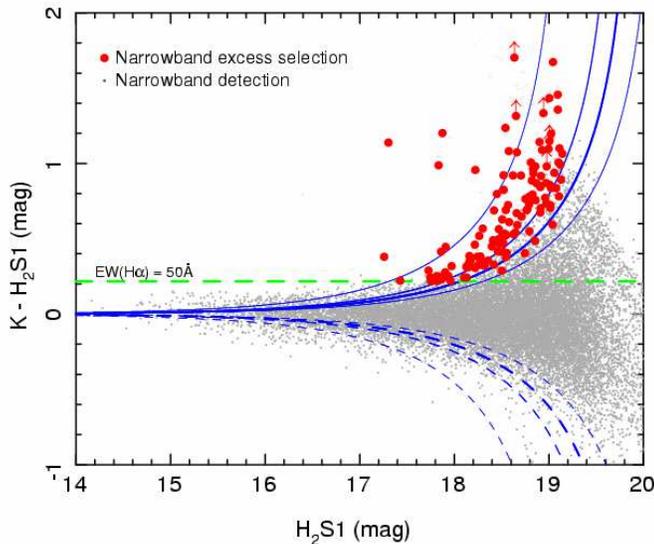
Figure 1. The $K - H_2$S1 colour-magnitude diagram used to select narrow-band excess objects, and thus possible $z = 2.23$ Hα emitters. Narrow-band colours have been corrected to account for broad-band continuum slope using the $(z-K)$ broad-band colour (see §3.1). $\Sigma = 2, 2.5, 3$ & 5 selection cuts are shown, as is a 50Å minimum in equivalent width used to select significant emitters. The Σ cuts here are averaged over the whole field area, but these change slightly for each WFCAM tile as we take into account individual frame zeropoints and noise properties (although there is only a small variation over the survey). We show all detections that have would been selected as narrow-band excess sources as filled circles (limits indicate that source was not detected in the broad-band frame). These narrow-band excess sources are subject to a further selection described in more detail in §3.2.

Figure 2. Three examples of narrow-band excess sources of various significance, Σ. The top, middle and lower panels show $\Sigma \sim 5$, $\Sigma \sim 3$, $\Sigma \sim 2.5$ respectively. The left hand panels show the K-band continuum, the centre shows the H$_2$S1 narrow-band image, and the right shows the continuum-subtracted narrow-band image. The K-band image has been scaled to account for the filter widths and both frames were locally registered with improved astrometric accuracy and smoothed with a Gaussian kernel to the same effective seeing. Images are $30'' \times 30''$ square and orientated North up and East left and scaled identically. Note that all images have been re-binned to the scale of the K-band frame: $0.4''$/pix.

than many extended sources, therefore we construct flats for each position in the micro-stepped sequence separately as if they are part of a standard dither.

A world coordinate system is fit to each frame by querying the USNO A2.0 catalogue, fitting on average ~ 100 objects, and then frames are aligned and co-added with SWARP[1] (this performs a background mesh-based sky subtraction, optimised to provide the best representation of the large scale variations across the field). In the case of the micro-stepped (narrow-band images), this step is preceded by drizzling the frame onto a grid with a pixel scale of $0.2''$ (i.e. half the camera pixel scale).

WFCAM frames suffer from significant cross-talk, manifesting itself in toroidal features at regular (integer multiples of 128)

pixel intervals from sources in the read-out direction. As these are tied to the positions of real objects, they are not removed by dithering the frames. High order cross-talk can easily mimic real objects, therefore these positions are flagged at the catalogue stage; we discuss this further in §3.

Broad and narrow-band frames are calibrated by matching $10 < K < 15$ stars from the 2MASS All-Sky Catalogue of Point Sources (Cutri et al. 2003) which are unsaturated in our frames. Since the narrow-band filter falls in the K-band, we can check the zero-point offsets to be applied to the narrow-band frames directly from the broad-band calibration, taking into account the relative widths of the filters, such that the offset between the zeropoints is $2.5 \log(\Delta\lambda_K / \Delta\lambda_{H_2S1})$. As an additional verification, we check that $K - H_2$S1 ~ 0 as expected using the photometry of the bright stars. We estimate our absolute K calibration is good to $\lesssim 1\%$ from the scatter compared to 2MASS[2]

---

[1] Both SWARP and SEXTRACTOR are distributed by Terapix (http://terapix.iap.fr) at the Institut d'Astrophysique de Paris.

[2] An independent data reduction of a sub-set of the science frames by the

2.3 Source extraction and survey limits

Our survey is made up of a mosaic of three WFCAM paw-prints, i.e. twelve $13.7' \times 13.7'$ tiles. Sources are detected and extracted using SEXTRACTOR (Bertin & Arnouts 1996). A final narrow-band catalogue is made by matching detections in the H_2S1 to the broad-band image. Since the frames are well aligned astrometrically, a simple geometric matching algorithm suffices, with a maximum search radius of $2''$. Cross-talk artifacts in WFCAM frames can mimic the narrow-band excess objects we are selecting for. Therefore, to clean the catalogue from possible cross-talk contaminants we measure the chip (x, y) position of bright sources, and flag regions at integer multiples of 128 pixels along the direction of readout. These chip positions can be converted to a sky coordinate and then compared to the narrow-band catalogue. As a rule, we remove an object from the catalogue if it lies within $2''$ of any cross-talk position. Note that by avoiding the zeroth order cross-talk position, we also avoid spurious detections close to bright stars (although in this case the exclusion radius is larger to account for extended halos and diffraction spikes, at $30''$). Due to the lower exposures received by the edges of the individual frames (caused by the jitter pattern), we ignore detections from within $\sim 10''$ of any frame edge. The total area lost due to cross-talk and star masking is negligible ($< 0.1\%$), however including the edge-clipping we survey an effective area of 0.603 square degrees.

Due to the fact that the observations were acquired over a long period of time, with slightly different seeing and exposure times (Table 1), we treat each tile separately, detecting objects down to each tile's limit. The average 3σ depth of the broad-band frames is $K = 20.1$ mag; we detect a total of 19079 objects down to this limit across 0.603 sq. degrees. Note that all magnitudes are measured in $3''$ diameter apertures, and this recovers the majority of the flux.

To confirm the depth and completeness of the images, we perform Monte Carlo simulations of the detection of a large number of 'fake' sources (a single Gaussian point source generated with IRAF's ARTDATA with a FWHM matching the image PSF). By scaling the artificial source over a range of known flux, and inserting at random locations over the frames, we measure the detection rate (i.e. the completeness) as a function of observed magnitude using an identical extraction procedure to that used to generate the main catalogue. We use this detection completeness information to correct the derived luminosity function of $H\alpha$ emitters.

3 SELECTION TECHNIQUE

3.1 Narrow-Band excess selection

Potential $z = 2.23$ $H\alpha$ emitting candidates are initially selected based on the significance of their narrow-band excess, i.e. their $K - H_2S1$ colour. Galaxies with a strong emission line falling in the narrow-band filter will have $H_2S1 < K$. The significance of the narrow-band excess can be parameterised in terms of Σ, which quantifies the excess compared to what would be expected for a source with a flat spectrum (Bunker et al. 1995). This parameter is similar to a standard signal-to-noise selection, and we chose to select candidate emitters with $\Sigma > 2.5$. This is equivalent to a colour of:

$$m_K - m_{H_2S1} = -2.5 \log \left[1 - \Sigma \delta 10^{-0.4(c - m_{H_2S1})} \right] \tag{1}$$

Cambridge Astronomical Survey Unit (CASU) confirms consistent photometry (M. Riello private communication).

where c is the zeropoint of the narrow-band image and δ is the photometric uncertainty. The $H\alpha$ line flux $F_{H\alpha}$ and equivalent width $W_{H\alpha}$ can be calculated:

$$F_{H\alpha} = \Delta\lambda_{H_2S1} \frac{f_{H_2S1} - f_K}{1 - (\Delta\lambda_{H_2S1}/\Delta\lambda_K)} \tag{2}$$

and

$$W_{H\alpha} = \Delta\lambda_{H_2S1} \frac{f_{H_2S1} - f_K}{f_K - f_{H_2S1}(\Delta\lambda_{H_2S1}/\Delta\lambda_K)} \tag{3}$$

where $\Delta\lambda_K$, $\Delta\lambda_{H_2S1}$ are the widths of the broad and narrow-band filters and f_K and f_{H_2S1} are the flux densities in the two filters. $W_{H\alpha}$ is simply the ratio of the line flux and continuum flux density, and will also include contribution from the adjacent [NII] line. However, we calculate the expected $H\alpha$ line flux by assuming $F_{[NII]}/F_{H\alpha} = 0.33$ for extragalactic HII regions (Kennicutt & Kent 1983) and correcting appropriately. Note that this may result in conservative $H\alpha$ fluxes, since for metal-poor galaxies this contribution may be lower.

In Figure 1 we present the colour-magnitude diagram with selection criteria. Some care must be taken in deciding on the selection, and we briefly describe it here. Firstly, we only use narrow-band detections with detection significances of $> 3\sigma$. It is not necessary that the source is also detected in the broad-band frame, and we assign an upper limit if there is no corresponding continuum detection. We define an initial selection criteria of $\Sigma > 2.5$ (this is a function of narrow-band flux and combined error due to sky noise in both the broad and narrow-band images, as described above). We account for bright foreground objects with steep continua across the K-band by making use of the $z - K$ colours available for all detections from the COSMOS archival z-band imaging (Capak et al. 2007). Their very red continua will result in a larger effective wavelength for the broad-band detections. We correct for this to make a better estimate of the continuum contribution to the narrow-band flux at the 2.121μm. We measure $K - H_2S1$ as a function of $(z - K)$, and fit the data with a linear trend using a least squares fit. The slope of this line is then be used to correct the $K - H_2S1$ colour. We find that on average the correction factor to the narrow-band magnitude excess is $0.03(z - K)$. To account for narrow-band detections that have large significance but low equivalent widths (e.g. van der Werf et al. 2000), we enforce an additional selection criteria of $W_{H\alpha} > 50$Å. This is an arbitrary threshold, but is chosen to reflect the general scatter about $K - H_2S1 = 0$ (see Figure 1).

The $H\alpha$ line-flux limit is the theoretical minimum that could be detected taking into account all these selection criteria. The average 3σ $H\alpha$ flux limit over the survey is 1×10^{-16} erg s^{-1} cm^{-2}. As a final quality control check, we visually inspect each candidate in order to filter any remaining erroneous sources (for example, non-crosstalk associated artifacts, etc.). In Figure 2 we present the narrow-band field around three candidate emitters representing a range of detection significance ($2.5 \lesssim \Sigma \lesssim 5$). For each panel we show the narrow-band frame before and after continuum subtraction using the broad-band image after suitably scaling to account for the relative filter widths. We detect a total of 180 sources meeting the narrow-band selection criteria across 0.603 square degrees.

3.2 Broad band colours: further selection, redshift confirmation and line contamination estimates

We must be certain that the selection in colour space is actually identifying the $H\alpha$ line at $z = 2.23$ rather than another strong emis-
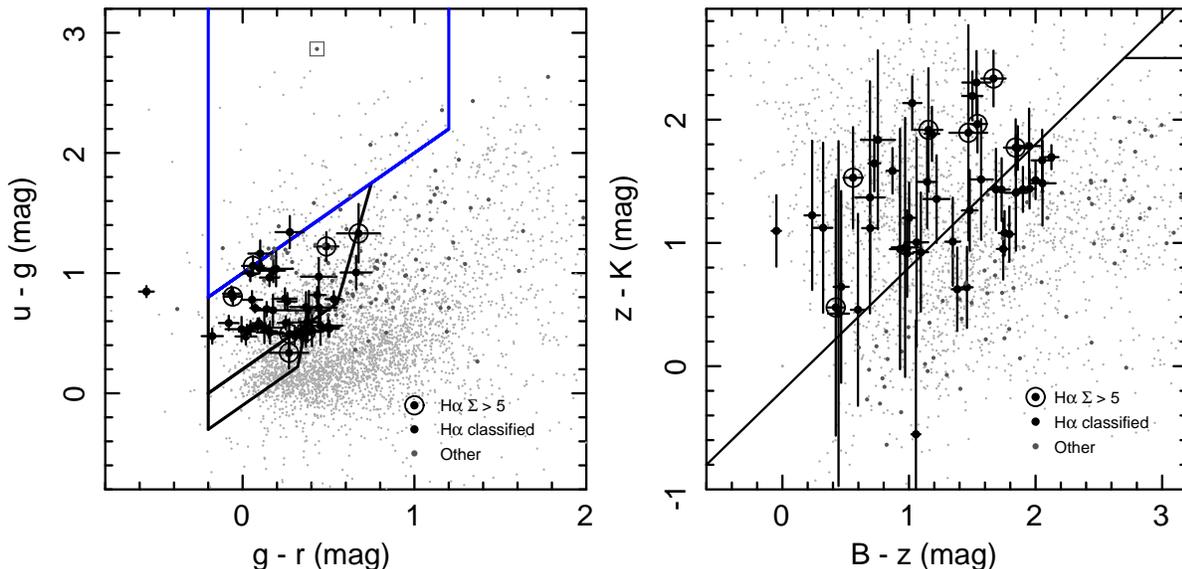
Figure 3. Broad-band colours of narrow-band selected objects from our survey. (left) *ugr* colours with the LBG and BM/BX selection criteria of Steidel et al. (2003) (right) *BzK* colours divided into high redshift starforming galaxies (*sBzK*) and high redshift passive galaxies (*pBzK*) and foreground galaxies, using the selection of Daddi et al. (2004). In both cases we compare to a 1-in-100 sampling of the general colour distribution using photometry available for the COSMOS field. It is clear that the straightforward narrow-band selection outlined in §3.1 is also detecting low redshift galaxies, and we require further selection with broad-band colours to identify these. However, the low redshift detections likely correspond to *real* emission lines, and we discuss this further in §3.2. Large points indicate our secure Hα emitters after employing our secondary colour selection outlined in §3.2 and we highlight the high significance ($\Sigma > 5$) candidates, noting that all of these fall in the *sBzK* and BX/BM selection regions. For clarity, we only show photometric uncertainties for Hα candidates.

sion line at another redshift. At higher redshift, the most important contaminant is [OIII]$\lambda5007$ at $z = 3.23$ (although these objects are interesting in their own right as possible examples of high-z AGN or star-forming galaxies). At low redshift, we are potentially susceptible to any strong line with an emission wavelength between Hα and H$_2$S1.

The most robust way to confirm the selection is through follow-up spectroscopy which can unambiguously identify the lines. However, complete spectroscopic follow up (at least in the short-term) is unfeasible. A 'cheaper' alternative is to make use of extensive multi-band optical/near-infrared photometry available for COSMOS (Capak et al. 2007), which can be used to improve the Hα selection. Unfortunately, at $z = 2.23$ the current photometric redshifts are not reliable enough to confirm Hα emission (Mobasher et al. 2007), so we turn to the cruder method of colour/colour-selection to clean our high redshift sample.

We therefore define a secondary optical selection, tuned according to the colours of a sub-sample of high significance ($\Sigma > 5$) Hα candidates from the pure narrow-band selection. To discriminate between high and low redshift emission line galaxies, we first use the *sBzK* selection first presented by Daddi et al. (2004), and now becoming popular to select active galaxies at $z > 1.4$. An alternative selection of high redshift galaxies is made with *ugr* colours, and has been used to search for $z \sim 3$ Lyman Break galaxies (LBGs, Steidel et al. 1996) and 'BM/BX' star-forming galaxies at $z \sim 2$ (Adelberger et al. 2004, Steidel et al. 2003). We use the BM/BX selection as a further indicator that the narrow-band selected galaxies are at high redshift (additionally the LBG selection can also be used to detect possible $z \sim 3$ [O III]$\lambda5007$ emitters). Candidate Hα emitters are narrow-band excess objects which also satisfy the BM/BX selection *or* the *sBzK* selection. In a further effort to eliminate foreground contaminants we impose a magnitude

cut of $z < 22.5$ (equivalent to $M_u < -23.7$ at $z = 2.23$). This yields a total Hα sample of 55 compared to our original selection of 180 sources on the basis of narrow-band selection alone. We present the colour-colour plots with selection criteria in Figure 3. After the colour selection, the majority of Hα emitters fall in both the BM/BX and *sBzK* regions, with those that do not having large enough photometric errors that place them $< 1\sigma$ away in colour-space. Note that two objects flagged as Hα emitters are potentially low-redshift [FeII]$\lambda1.64$ emitters based on their photometric redshifts (see Figure 4 and discussion below). Thus, the photometric selection is not a fool-proof method, although it suggests the contamination rate is low ($\lesssim 3\%$). To estimate the number of galaxies that could have been potentially missed by this further colour selection, we Monte Carlo our selection by allowing the photometry to vary randomly in a range defined by the (1σ) uncertainty on each point, then count the number of galaxies satisfying the Hα criteria and compare this to the nominal value. Repeating this procedure many times builds up a measure of the the likely contamination/incompleteness as galaxies are scattered in and out of the selection regions. Our results suggest that the number of galaxies missed (or alternatively the interloper fraction) could be as much as 10%. Assessing this contamination more accurately will require follow-up spectroscopy, which at the time of writing, is underway.

What are the remaining narrow-band excess objects which fail our colour selection? At least one appears to be a high redshift (possibly [OIII]$\lambda5007$) emitter selected in the LBG cut, but the bulk of the remaining objects are likely to be low-redshift given their colours. There are several other low redshift emission lines that could potentially be detected, and to investigate this, in Figure 4 we plot the probability distribution $P(z)$ of $z_{\rm phot}$ of (a) candidate Hα emitters, (b) Paα and Paβ candidates and (c) unclassified remaining narrow-band excess detections. Using a conservative pho-

tometric redshift uncertainty of $dz = \pm 0.05$ we identify 12 Paα and 6 Paβ candidates. In the unclassified redshift distribution there are two clear peaks in the distribution at $z \sim 0.4$ and $z \sim 0.9$. The low redshift emitters could potentially be [FeII]$\lambda 1.6 \mu$m or several Brackett lines, whereas the slightly higher redshift peak might correspond to Paγ. Clearly this must be confirmed through spectroscopy, but it appears that the narrow-band selection is detecting real line-emitters, but is not sufficient alone to isolate Hα at $z = 2.23$. Identification of lower redshift interlopers will become easier when more accurate photometric redshifts are available for COSMOS (Mobasher et al. 2007 & private communication).

To check for contamination for higher-z line emitters, we use a *ugr* cut to select $z \sim 3$ Lyman Break galaxies (LBGs), and so identify possible [OIII]$\lambda 5007$ contaminants (Figure 3). In our total narrow-band selected sample, only one object satisfies the LBG selection criteria, and therefore we conclude that the $z = 3.23$ [OIII]$\lambda 5007$ contamination rate is negligible for our sample. We note that in a follow up spectroscopic survey of narrow-band identified $z = 2.2$ Hα emitters by Moorwood et al. (2000), six of 10 candidates were confirmed as $z = 3.23$ [OIII]$\lambda 5007$. Thus it is not clear whether environmental effects are responsible for the high contamination observed in this previous small scale survey.

Finally we assess the impact of contamination from AGN at $z = 2.23$ which would impact on our assessment of $\rho_{\rm SFR}$ from the Hα LF. We are probing the expected peak in the SFRD, but this is also associated with the peak of AGN activity (Shaver et al. 1996; Boyle & Terlevich 1998) – what is the expected contamination rate in our Hα selected sample? As with contamination from emission lines at different redshifts, without spectroscopic information (for example the Hα/[NII] ratio discriminating between star-formation and nuclear activity), we must address this issue statistically. As described by van der Werf et al. (2000), the AGN interloper fraction is likely to be low: the fraction of AGN in local Hα selected galaxies is <5% (Gallego et al. 1995), and this is not likely to increase toward high redshift (Teplitz et al. 1998). On the other hand, Shioya et al. (2008) include a 15% correction for AGN contamination in the Hα luminosity function at $z = 0.24$, based on the results of Hao et al. (2005) who studied the Hα luminosity density from AGN in the Sloan Digital Sky Survey. We adopt this same 15% AGN contamination in our measurement, resulting in a more conservative estimate of $\rho_{\rm SFR}$.

3.3 Spectroscopic comparison

The *z*COSMOS survey (Lilly et al. 2007) is an extensive spectroscopic project obtaining thousands of redshifts in the COSMOS field. To search for any existing spectra corresponding to our narrow-band excess sample, we cross-correlate our catalogue with the current *z*COSMOS spectroscopic catalogue (S. Lilly priv. comm.). We do not expect a large degree of overlap between our catalogue and *z*COSMOS, since we are detecting relatively faint galaxies, and indeed there were only five matches with secure redshifts. One Hα candidate is included in the 'faint' *z*COSMOS catalogue and confirmed to securely lie at $z = 2.2329$, verifying the selection at least for this candidate. The remaining matches are all in the 'bright' sample. Three of these were identified by us as being possible Paα at $z \sim 0.13$, and indeed two have confirmed redshifts of $z = 0.1312$ and $z = 0.1298$, although another has $z = 0.1086$. The final match has $z = 0.7340$, and it is unclear if this corresponds to a real emission line. Although this is a very limited spectroscopic confirmation, it does suggest that we are detecting a range of emission lines, and that our secondary filtering
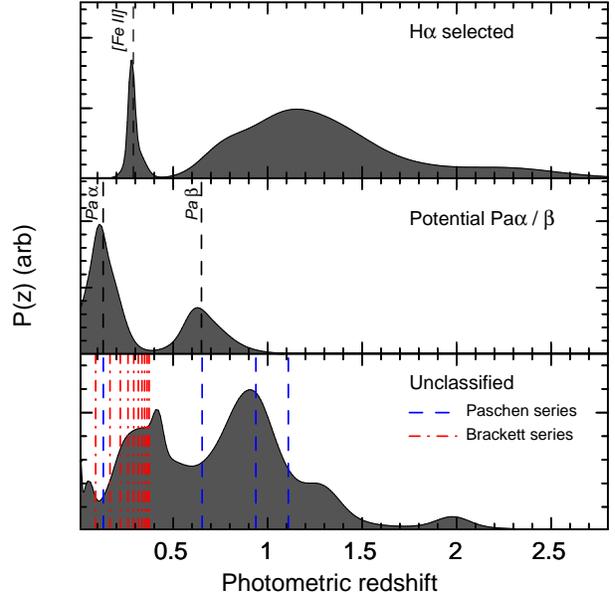
Figure 4. The summed probability distributions $P(z)$ for photometric redshifts: (top) narrow-band excess detections satisfying our *ugr*/*BzK* selection. Note that there is a spike in $P(z)$ at $z \sim 0.3$, corresponding to the redshift of [FeII]$\lambda 1.64$ in the H$_2$S1 filter. This spike represents two objects and these are removed from our sample. The broad distribution of $z_{\rm phot}$ at $z \gtrsim 1$ are probably real Hα emitters with poorly determined photometric redshifts; (middle) distribution of galaxies selected as Paα and Paβ emission lines with $z_{\rm phot} = 0.13 \pm 0.05$ and $z_{\rm phot} = 0.65 \pm 0.05$ respectively; (bottom) remaining 'unclassified' emitters. There are two main peaks to the distribution of unclassified objects: at $z \sim 0.3$ which could correspond to [FeII]$\lambda 1.64$ or several Brackett lines. At $z \sim 0.8$ the peak could correspond to Paγ.

technique is useful for weeding out low redshift interlopers. We note that our near-infrared spectroscopic follow-up will allow us to make a much better estimation of the contamination rate.

4 RESULTS

We detect a total of 55 robust candidate $z = 2.23$ Hα emitters over 0.603 square degrees of the COSMOS field, resulting in a surface density of $91 \pm 10 \deg^{-2}$ above a flux limit of $1 \times 10^{-16} \, {\rm erg \, s^{-1}}$, equivalent to a SFR of $30 \, M_\odot \, {\rm yr^{-1}}$ at this redshift. In the following sections we briefly discuss their multi-wavelength and morphological properties, and use the sample to evaluate the Hα luminosity function and thus star-formation rate density at $z = 2.23$. Finally, we make an estimate of the real space correlation length of Hα emitters by measuring their two-point angular correlation function.

4.1 Hα luminosity density at $z = 2.23$

4.1.1 Evaluating the luminosity function of Hα emitters

To calculate the luminosity function of Hα emitters, we convert line fluxes to luminosities, correcting for 33% [NII] contribution to the measured flux. The volume is reasonably well defined by the survey area and narrow-band filter width (50% cut-on/off: 2.111–2.132μm), which probes a co-moving depth of $\sim$40 Mpc, and is equivalent to $220 \times 10^3 \, {\rm Mpc}^3$ (co-moving). However the reader

should note that since the narrow-band transmission function is not a perfect top-hat, the effective volume probed will vary as a function of intrinsic luminosity, with more luminous Hα emitters being detected over a larger volume than fainter sources. Similarly, the incompleteness will vary strongly as a function of apparent luminosity, since faint Hα emitters at redshifts corresponding to the low-transmission wings of the narrow-band filter might be lost, and bright lines will have their luminosity underestimated, contributing to the counts in lower luminosity bins. To estimate the impact of this effect on our measured results, we model these observational effects on a 'true' model luminosity function. Our simulation consists of a set of model Hα emission lines convolved with the H2S1 transmission function, where the lines are randomly placed in a redshift range corresponding to the full width of the filter. After convolving 1000 such lines per luminosity interval, we recover the effective volume probed, the incompleteness and luminosity biases (i.e. including intrinsically bright emitters dimmed by the edge of the transmission function falling in lower luminosity bins). The combination of these effects modifies the model luminosity function, the main change being a ~10% reduction in the faint-end slope α and a ~20% decrease in $\phi^\star$ compared to a uniform transmission model. The effect on $L^\star$ is negligible. As we describe below, since we fix the faint end slope $\alpha = -1.35$, the difference in the integrated luminosity function above the simulated detection threshold is slightly less than if this was a free parameter, ~10%, and we correct for this difference in our measurement of ρ_{SFR}.

Although Hα is relatively insensitive to dust extinction (unlike Lyα, it is not resonantly scattered), dust absorption must still be taken into consideration when deriving luminosities. A robust technique would be to obtain spectroscopy of each source to measure the Balmer Hα/Hβ decrement, but this is not currently feasible for our sample. Instead we simply adopt $A_{\mathrm{H}\alpha} = 1$ mag (Kennicutt 1992; 1998), as is applied in similar earlier studies (Fujita et al. 2003; Pascual et al. 2005; Ly et al. 2007) for SFR estimates. Although it is known that the specific extinction is a function of SFR (Jansen et al. 2001; Aragón-Salamanca et al. 2003; Hopkins et al. 2001), for ease of comparison with other samples, we apply this constant correction to our sample, noting that in the cases where the actual extinction is higher, our measured SFRs will be conservative. We compare SFR indicators for our sources in §4.2.2 and confirm that the correction used here is appropriate.

Our LF has been corrected for completeness on a bin by bin basis using the completeness functions estimated from the narrow-band simulation (§2.3), and the lower luminosity limits have been dealt with by performing a survival analysis on the binned data, using the probability estimator of Avni et al. (1980). Note that we apply a correction for the incompleteness caused by the shape of the H2S1 transmission described above on the integrated luminosity function (see §4.1.2). The errors are derived from the Poisson statistics of each bin, although we apply a slightly more conservative bootstrap analysis to estimate the uncertainties on the fit values, described in more detail below. We fit the LF with a Schechter function characterised by α, $\phi^\star$ and $L^\star$: $\phi(L)\mathrm{d}L = \phi^\star(L/L^\star)^\alpha \exp(-L/L^\star)\mathrm{d}(L/L^\star)$. Since we lack sufficient depth to fit the faint end slope, we fix $\alpha = -1.35$, the value observed by Gallego et al. (1995) for their $z = 0$ Hα study. This approach was also used by Yan et al. (1999) for the Hα LF at $z = 1.3$. Therefore we cannot show any evolution in the faint end slope of the Hα LF – a deeper survey is required for this. In fact Reddy et al. (2007) find evidence for a steeper faint end slope for UV/optical colour-selected star-forming galaxies at high redshifts ($z \sim 2$–3).
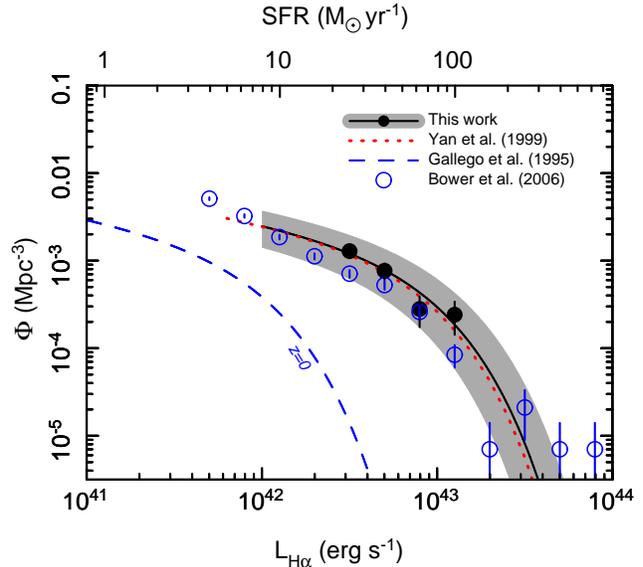

Figure 5. Hα luminosity function from this work compared to those derived at $z = 0$ (Gallego et al. 1995) and $z = 1.3$ (Yan et al. 1999) (these are not corrected for dust extinction). Errors are based on the Poisson counting error and the completeness correction applied to each bin, derived from the detection rate of narrow-band selected sources. The luminosity function is fit with a Schechter function with a fixed faint end slope, $\alpha = -1.35$ (identical to Yan et al. 1999 and Gallego et al. 1995) – deeper observations will be required to probe the evolution of the faint end slope of the luminosity function. Our results show significant evolution from $z = 0$ equivalent to an order of magnitude in luminosity evolution. Our LF is also very similar to the $z = 1.3$ Hα luminosity function, consistent with little or no evolution between $z = 2.23$ and $z = 1.3$, interpreted in terms of the star formation rate density as a peak or plateau occurring at $z \sim 2$ (see Figure 6). We compare to the theoretical prediction of the luminosity distribution of Hα emitters from the Bower et al. (2006) variant of the semi-analytic GALFORM code (Cole et al. 2000). The observed counts agree well with the model, although there are hints that the faint end slope is slightly steeper than our assumed value.

Adopting a $\alpha < -1.35$ would obviously have a rather dramatic effect on extrapolated values for ρ_{SFR}, which we discuss in §4.1.2.

To estimate uncertainties on the LF, we refit the Schechter function by bootstrapping, with the variance of the resulting parameters forming our uncertainty in $\phi^\star$ and $L^\star$. We find $\phi^\star = (1.45 \pm 0.47) \times 10^{-3}$ Mpc^{-3} and $\log L^\star = 42.83 \pm 0.13$ erg s^{-1}. We present the results in Figure 5 in comparison to lower redshift studies of the Hα LF $z = 0$, demonstrating the sharp increase in Hα emitters from $z = 0$–2.23. Our results are very similar to the luminosity distribution found by Yan et al. (1999), suggesting that there is little evolution of the bright end of the Hα LF across the 2 Gyrs between $z = 2.23$ and $z = 1.3$.

4.1.2 The star-formation rate density at z = 2.23

Next we use the integral of the LF to find the volume averaged star-formation rate density, ρ_{SFR}. In Figure 6 we present the evolution of ρ_{SFR} out to $z = 2.23$ using Hα *only*. In order to compare results, we take the LF parameters for Hα surveys compiled by Hopkins (2004) and integrate these down to $L_{\mathrm{H}\alpha} = 10^{42}$ erg s^{-1}, the approximate luminosity limit of the present survey. To convert Hα luminosity to a star-formation rate, after applying a factor 2.5 to $L_{\mathrm{H}\alpha}$ to account for $A_{\mathrm{H}\alpha} = 1$ mag,
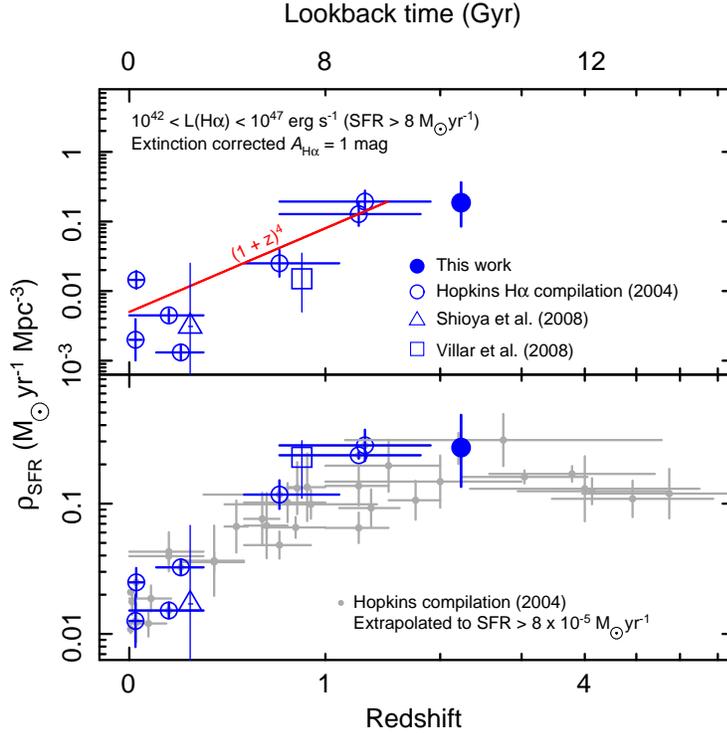
Figure 6. The evolution of the star-formation rate density out to $z = 2.23$ using the Hα tracer alone, and compared to a heterogeneous mix of multi-wavelength tracers (all converted to the cosmological parameters used throughout this work). The data are collected taken from the compilation of literature data made by Hopkins (2004), and recent works of Shioya et al. (2008) and Villar et al. (2008). Where corrected for extinction, are modified by a common factor $A_{H\alpha} = 1$ mag. In the top panel, we calculate the integrated Hα luminosity down to the approximate luminosity limit of the present survey, $L_{H\alpha} > 10^{42}$ erg s^{-1}. Our results support a flattening of the ρ_{SFR} between $z \sim 1$–2. In the bottom panel we apply the same integration range as Hopkins (2004), extrapolating down to $L_{H\alpha} > 10^{37}$ erg s^{-1}. The general evolution of ρ_{SFR} is mirrored here, but the reader should be aware of the potentially strong impact uncertainties in the faint end slope have on the integrated luminosity function. Surveys of high-redshift star-forming galaxies have yet to satisfactorily constrain this parameter.

we use the standard calibration of Kennicutt (1998); $\mathrm{SFR}[H\alpha] = 7.9 \times 10^{-42}(L_{H\alpha}/\mathrm{erg\,s}^{-1})\,M_\odot\,\mathrm{yr}^{-1}$ (assuming continuous star formation, Case B recombination at $T_e = 10^4$ K and a Salpeter initial mass function [IMF] ranging from 0.1–100$M_\odot$). Correcting for the transmission incompleteness described in §4.1.1 and a 15% correction for AGN contamination (Shioya et al. 2008), we find $\rho_{SFR} = 0.17^{+0.16}_{-0.09}\,M_\odot\,\mathrm{yr}^{-1}\,\mathrm{Mpc}^{-3}$ where the uncertainty is equivalent to the 1σ uncertainties on the luminosity function fit parameters. Our results support a flattening or peak in the level of star-formation activity between $z \sim 1$–2.

In Figure 6 we also show the evolution of ρ_{SFR}, but extrapolated to a much fainter luminosity, $L_{H\alpha} > 10^{37}$ erg s^{-1} (SFR $> 8 \times 10^{-5}\,M_\odot\,\mathrm{yr}^{-1}$), in line with the ρ_{SFR} compilation of Hopkins (2004). We remind the reader of the uncertainty inherent in interpreting ρ_{SFR} estimates derived from such extrapolations: the uncertainty in the slope of the faint end of the luminosity function could have a dramatic effect on the result. For this extrapolated case (again, corrected for extinction), we find $\rho_{SFR} = 0.25^{+0.20}_{-0.13}\,M_\odot\,\mathrm{yr}^{-1}\,\mathrm{Mpc}^{-3}$. This is in broad agreement with the range of ρ_{SFR} estimates (for a variety of tracers) at $z = 2.23$ (Fig. 6) and confirms the plateau in ρ_{SFR} above $z \sim 1$.

Our measurements of ρ_{SFR} are consistent with the results of Reddy et al. (2008), who estimate the Hα luminosity density at $1.9 \leqslant z < 2.7$ by using the correlation between dust-corrected ultra-violet and Hα SFRs (Erb et al. 2006). They find $\rho_{SFR} = 0.35 \pm 0.09\,M_\odot\,\mathrm{yr}^{-1}$ over this (albeit larger) redshift range. Reddy

et al. (2008) measure a steeper faint end slope for the ultraviolet luminosity density at $z \sim 2$, $\alpha = -1.88$. If this behaviour is reflected in the general star-forming population at this redshift, then we would also expect a steeper Hα faint end slope. This would increase the extrapolated ρ_{SFR} presented here. For example, fixing $\alpha = -1.65$ (more in line with the theoretical luminosity distribution from Bower et al. 2006), ρ_{SFR} would increase by nearly a factor of 2. This should be taken as a cautionary point by the reader, when interpreting our extrapolated results.

There is a final caveat regarding the luminosity function presented in Figure 5; namely the treatment of dust. In this analysis we have assumed a uniform correction, $A_{H\alpha} = 1$ mag for ease of comparison with other results (we discuss the validity of this assumption in §4.2.2). Note that, in reality, this correction may be a function of luminosity, such that the most luminous systems require larger corrections. This would have most effect on the bright end of the LF, where we suffer the most from low-number statistics.

4.1.3 Comparison to theoretical predictions of the luminosity distribution

Recent recipes for galaxy formation using a semi-analytic prescription provide us with the opportunity to directly compare observed Hα line luminosities with theoretical predictions (Bower et al 2006). In Figure 5 we present the Hα luminosity function at $z = 2.23$ from the Bower et al. (2006) model (hereafter 'B06
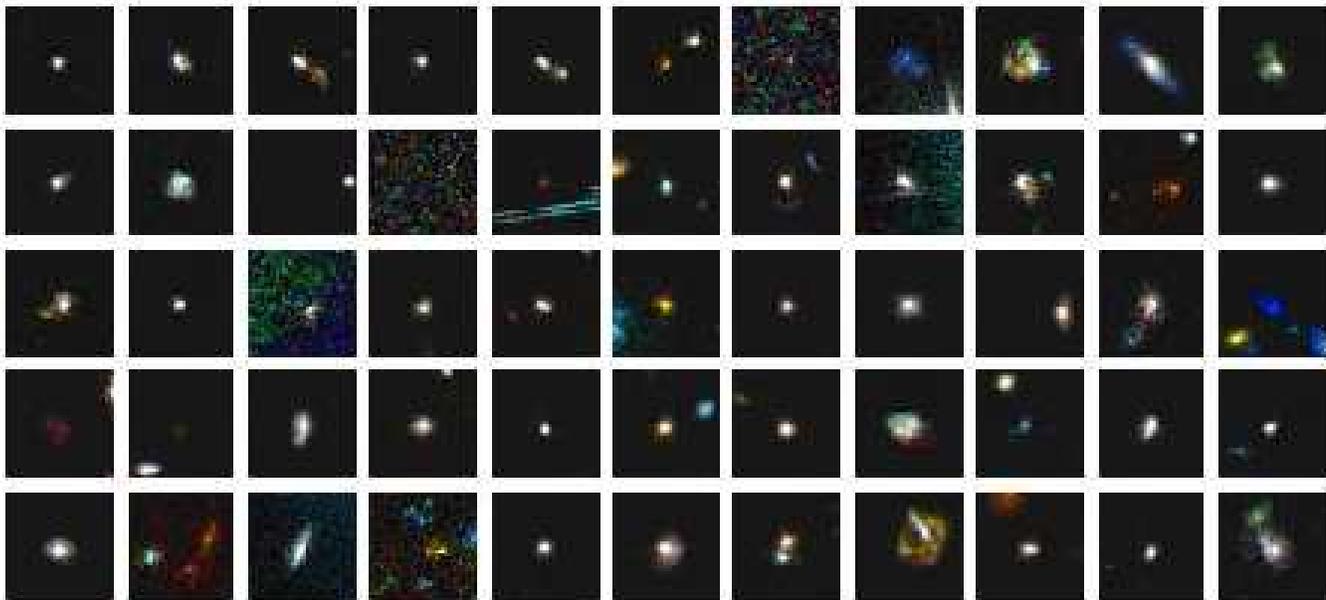
Figure 7. $5'' \times 5''$ *HST* ACS thumbnail images of the 55 $z = 2.23$ Hα candidates. The images are coloured with a map generated from the ground based *Brz* imaging, and use the F814W filter as a luminance channel (all images are scaled identically and orientated with north up and east to the left). Note that at $z = 2.23$, $5''$ is equivalent to ~40 kpc in projection. The images are organised row-wise in order of decreasing Hα luminosity such that the top left thumbnail is the most luminous, and the bottom right is the least. There are two types of morphology: very compact or more extended (generally disturbed) systems. Many of the disturbed morphologies show evidence for two bright components within ~ $1''$ of each other – indicative of recent or ongoing interaction which might be powering star-formation. The colour images appear to support this, with some of the more extended sources showing clear red and blue parts, reminiscent of merging star-forming galaxies in the local Universe.

model') which populates dark matter halos in the N-body Milli-Millennium simulation with model galaxies (1/16 the volume of the full Millennium simulation, Springel et al. 2005). The B06 model is a variant of GALFORM, the Durham semi-analytic code (Cole et al. 2000; Benson et al. 2003), which includes a new pre-scription for AGN feedback. Such feedback appears to be very important for preventing the cooling of baryons in massive galaxies, and thus steepening the bright end of the luminosity function (see Bower et al. 2006). We take the *total* Hα luminosity from the cat-alogue, and enforce the same equivalent width cut, $W_{\mathrm{H}\alpha} > 50$Åas in our narrow-band selection. No other constraint is placed on other observable parameters. The observed luminosity distribution gen-erally appears to agree well with the predictions, although there appears to be a slight excess of bright Hα emitters in the model. The origin of this disparity could be caused by Cosmic variance effects or over-production of bright star-forming galaxies in the simulations, exacerbated by the low-number statistics in the high-luminosity bins. Nevertheless, the overall rough agreement of the Hα luminosity density over the observed range is encouraging.

4.2 The properties of Hα emitters

4.2.1 *Hubble Space Telescope ACS imaging – morphologies*

In Figure 7 we present *Hubble Space Telescope (HST)* ACS F814W thumbnail images of the candidate Hα emitters. The exquisite imaging from *HST* allows their rest-frame UV morphologies to be examined, and we have used this, along with *BRz* Subaru Suprime-Cam optical imaging from the COSMOS archive to preserve mor-phological information and reveal colour gradients that vary on scales comparable to ground-based imaging resolution. For exam-ple this allows us to distinguish red and blue components in an in-

teracting galaxy. We observe four morphological types: compact and isolated galaxies ($33 \pm 8\%$); amorphous or disc morpholo-gies ($35 \pm 8\%$) and galaxies with obvious multiple components ($27 \pm 7\%$). Note that several of the galaxies have too poor S/N in the *HST* images to determine a classification ($5 \pm 4\%$). We note that the close-companion rate is only marginally above that for a similar K-band selected sample: 21% of $18 < K < 19.5$ galax-ies selected from the full COSMOS survey have an $I < 25$ mag neighbour within $2.5''$.

The mean half-light radius ($r_{1/2}$, an effective measure of galaxies' size) for the Hα emitters is $\langle r_{1/2} \rangle = 2.1 \pm 0.5$ kpc. How do these galaxies compare with other UV-selected systems at the same epoch? Erb et al. (2004) report morphologies and sizes for 13 'BX' galaxies at $z \sim 2$ in the GOODS-N field (although these galaxies were selected partially for their known elongation, see also Förster-Schreiber et al. 2006). The 'BX' galaxies appear to have qualitatively similar properties to many of the Hα selected galaxies in this work: clumpy, 'tadpole' features (see also Law et al. 2007). BX galaxies in the Erb et al. (2004) sample have $r_{1/2} = 1.9 \pm 0.5$ kpc, implying they have similar sizes (and qualita-tively similar morphologies) to Hα-selected star-forming galaxies at the same redshift.

4.2.2 *Spitzer 24μm and VLA 1.4 GHz observations – obscured star-formation*

The entire COSMOS field has been observed with the Multiband Imaging Photometer (MIPS) on the *Spitzer Space Telescope*. The 24μm flux at $z \sim 2.23$ probes polycyclic aromatic hydrocarbons (PAH) emission lines. In dusty star-forming galaxies at this red-shift, 24μm should be dominated by the prominent 7.7μm emis-

sion feature, and so should be a good indicator of obscured star-formation. To investigate the possibility that some of the Hα emitters are dusty luminous starbursts, we cross-correlate the Hα catalogue with the *Spitzer*-COSMOS (Sanders et al. 2006) MIPS 24μm catalogues using a simple matching radius of $2''$. Seven Hα emitters from our sample of 55 are detected in both the wide and deep 24μm MIPS maps (flux limits of 0.3 mJy and 0.06 mJy respectively) with a noise weighted average 24μm flux density of $\langle f_{24\mu m} \rangle = 0.20 \pm 0.03$ mJy.

In order to search for a statistical signature of mid-infrared emission from the whole sample of Hα emitters we stack the 24μm data in regions around the source positions (the Hα fluxes of 24μm detections are not significantly different from the overall Hα population, so we include these in the stack). The resulting stacked image yields a significant flux excess, $f_{24\mu m} = 0.11 \pm 0.01$ mJy. The uncertainty is derived by stacking 50×55 thumbnail images around random locations in the 24μm map, and measuring the scatter in the fluxes measured in identical apertures in each stack. The significant 24μm flux suggest weak mid-infrared emission in these star-forming galaxies. Since COSMOS was also observed at 70μm and 160μm with MIPS, we apply a similar stacking analysis for these wavelengths in an attempt to place constraints on the far-infrared properties of the Hα emitters. We do not find significant flux excess in either case, and so we define 3σ upper limits of $f_{70\mu m} < 2.1$ mJy, and $f_{160\mu m} < 9.2$ mJy.

How does the infrared luminosity compare to the Hα luminosity? To compare these two values we first estimate the total-infrared luminosity by normalising an M 82-like spectral energy distribution to the observed 24μm flux and integrating over 8–1000μm (the choice of SED is motivated by the discussion in §4.2.3). The SFR is estimated using the calibration of Kennicutt (1998), $\mathrm{SFR[IR]} = 4.5 \times 10^{-45} \left(L_{8-1000\mu m}/\mathrm{erg\,s}^{-1} \right) M_\odot\,\mathrm{yr}^{-1}$. We find $\mathrm{SFR[IR]} = 90 \pm 40\,M_\odot\,\mathrm{yr}^{-1}$, where the uncertainty is derived by recalculating the total infrared luminosity by introducing a 50% variation in the normalisation of the SED, since at $z = 2.23$ the 24μm flux probes the 7.7μm PAH emission line, and the fraction that this band can contribute to the total infrared flux can vary. How does this compare with the Hα measurements? Without applying any correction for extinction at Hα, we calculate the average $\mathrm{SFR[H\alpha]} = 40 \pm 20\,M_\odot\,\mathrm{yr}^{-1}$ (the uncertainty reflecting the 1σ scatter in Hα luminosities, and assuming $\mathrm{SFR[H\alpha]} = 7.9 \times 10^{-42} \left(L_{\mathrm{H\alpha}}/\mathrm{erg\,s}^{-1} \right) M_\odot\,\mathrm{yr}^{-1}$, Kennicutt et al. 1998). Including the canonical extinction correction of 1 mag, this rises to $\mathrm{SFR[H\alpha]} = 100 \pm 45\,M_\odot\,\mathrm{yr}^{-1}$ in good agreement with the SFR derived from the average infrared luminosity. As described above, the true level of extinction could be a function of luminosity, however this result suggests that our adoption of a constant reddening correction does not result in a significant underestimate of the SFR.

Four Hα emitters are formally detected in the 1.4 GHz VLA map of COSMOS (Schinnerer et al. 2004), with an average flux of $\langle f_{1.4\,\mathrm{GHz}} \rangle = 160 \pm 20\,\mu$Jy. Again, these objects' Hα fluxes are not significantly different from the general population, and so we employ the same stacking technique to find the 'average' 1.4 GHz flux for the sample. We find $f_{1.4\,\mathrm{GHz}} = 9.7 \pm 1.2\,\mu$Jy (the error is calculated in the same manner as the 24μm stack – i.e. repeating the analysis for randomly co-added thumbnail images). Parameterising the correlation between infrared and radio luminosity as $q_{24} = \log(f_{24\mu m}/f_{1.4\,\mathrm{GHz}})$ (see Ibar et al. 2008) we find $q_{24} = 0.7 \pm 0.2$. This value is in good agreement with the expected q_{24} for an M 82 SED at $z = 2.23$, $q_{24} = 0.6 \pm 0.1$ (Ibar et al. 2008) , and so converting the radio luminosity to a far-infrared lu-

minosity (and thus SFR) is consistent with our derived SFRs from the 24μm luminosity and extinction corrected Hα luminosity described above.

4.2.3 Average spectral energy distribution of Hα emitters

In Figure 8 we show the average spectral energy distribution of the Hα emitters. The optical/near-IR *uBVgrizK*+F814W+IRAC 3.6–8μm photometry is averaged over all the Hα emitters (weighted by the individual photometric errors) and then fit with a choice of Sa-d and burst spectral templates (Bruzual & Charlot 1993) redshifted to $z = 2.23$ using the HYPERZ photometric redshift code (Bolzonella et al. 2000). Note that the IRAC measurements are the $3''$ aperture fluxes corrected to total flux using the values suggested by the S-COSMOS team: 0.90, 0.90, 0.84 and 0.73 for the 3.6, 4.5, 5.8 and 8μm cameras respectively. Coverage of the rest-frame near-infrared is useful for improving the photometric redshifts of high redshift objects, since it allows the location of the 1.6μm stellar bump to be tracked (e.g. Sawicki 2002). The wavelength of this feature corresponds to the minimum opacity of H^- ions in the atmospheres of cool stars (John 1988), and thus is an indicator of the evolved ($\gtrsim 20$ Myr old) stellar population. The average 3.6–8μm SED agrees with the 1.6μm feature redshifted to $z = 2.23$. The data are well fit by an Sc spectral type template with a foreground screen reddening of $A_V = 1.0$ mag (this parameter was free to vary in the range $0 < A_V < 2$). This suggests the UV continuum in these sources may be slightly more obscured than we are assuming for the Hα line emission.

The good fit to the spectral template is compelling evidence that our narrow-band plus photometric selection is indeed identifying a population of $z = 2.23$ star-forming galaxies, and shows that improved photometric redshifts that make use of bands redward of K will help in improving the narrow-band selection (Mobasher et al. 2007). As IRAC is probing rest-frame near-infrared emission, we can estimate the stellar mass of these galaxies from the absolute rest-frame K-band luminosity. We estimate the rest-frame absolute K-band magnitude from the 5.8μm flux, $M_K = -25.4$ mag (AB magnitude). The stellar mass, $M_\star$, is estimated using a similar method to Borys et al. (2005), assuming $M_\star$ is equal to the integrated stellar mass at the age of the galaxy. Note that our template assumes a continuous star-formation history, with a Miller & Scalo (1979) initial mass function (a burst template does not provide a satisfactory fit to the observed photometry). If the K-band luminosity traces stellar mass, then $M_\star = 10^{-0.4(M_K - 3.3)}/(L_K/M)\,M_\odot$ where L_K/M is the mass-to-light ratio, and the factor 3.3 corresponds to the absolute solar K-band luminosity (Cox 2000). For continuous star-formation we estimate L_K/M from the description of Borys et al. (2005) who use the STARBURST99 stellar synthesis code (Leitherer et al. 1999) to find $L_K/M = 103(\tau/\mathrm{Myr})^{-0.48}$ for ages $\tau > 100$ Myr. The age returned from HYPERZ is 1 Gyr, similar to the mean age of $z \sim 2$ UV-selected star-forming galaxies in the survey of Erb et al. (2006). Adopting a realistic range in ages, 0.5–2 Gyr we find $M_\star \sim 6.1$–$11.5 \times 10^{10} M_\odot$. This is larger than the mean stellar mass of the sample in Erb et al. (2006), who find $M_\star = (3.6 \pm 0.4) \times 10^{10}\,M_\odot$, but the disparity between the two mass estimates may be simply due to the different derivation methods used: comparison of the spectral energy distributions to stellar synthesis models in Erb et al. (2006) versus simple age-dependent mass-to-light ratios here.

In addition to the UV–near-IR photometry, we also show on Figure 8 the longer wavelength data described above: 24μm, 70μm, 160μm and 1.4,GHz cm statistical detections and limits. For com-
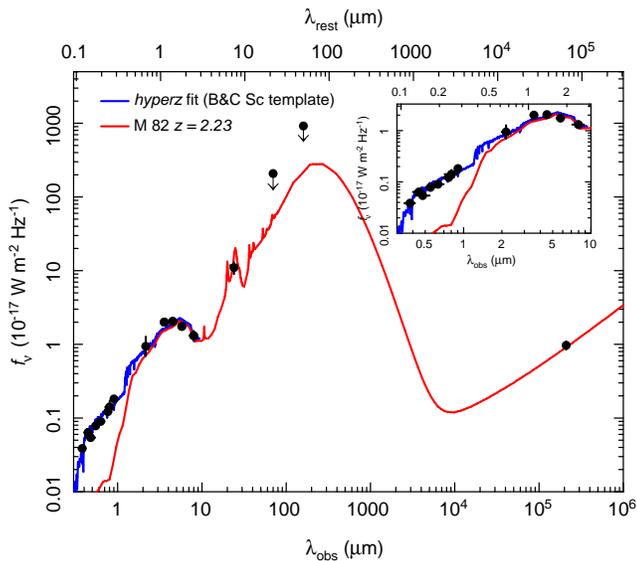
Figure 8. The average SED for Hα emitters based on UV–radio photometry from the COSMOS archive averaged over all 55 candidates. In the inset we fit these with a Sc galaxy template at $z = 2.23$ reddened by $A_V = 1$ mag. The fit agrees well with the average SED, suggesting that our narrowband selection is indeed identifying star forming galaxies at $z = 2.23$. The main panel extends the SED to longer wavelengths by stacking the 24μm, 70μm, 160μm and 1.4 GHz data (the 70μm and 160μm points are 3σ upper-limits), and we overlay the M 82 template, redshifted to $z = 2.23$ and scaled in flux accordingly. Again, this seems to verify the redshift selection, and suggests that the galaxies we select are similar to local starburst galaxies in their broad SEDs.

parison we show the M 82 galaxy SED (a local starburst) redshifted to $z = 2.23$ and scaled in flux to match the 24μm flux density accordingly. The average 24μm/1.4 GHz flux is consistent with what would be expected for a typical star-forming galaxy at $z = 2.23$ (Boyle et al. 2007; Ibar et al. 2008). This suggests that on average these galaxies are unremarkable starbursts, with SFRs $\lesssim 100\,M_\odot\,\mathrm{yr}^{-1}$, with properties broadly similar to the most actively star-forming galaxies found in the local Universe. We note however, that there is a departure from the similarity to M 82 in the rest-frame UV, with our composite SED showing quite significant UV-excess over what would be expected from M 82 at this redshift (Ibar et al. 2008). We interpret this as indicating that perhaps on average, the observed Hα emitters are not as dusty as the local LIRG, or they simply have higher escape fractions of UV photons.

4.3 Clustering of Hα emitters

4.3.1 Evaluating the clustering strength

Estimating the clustering properties of star-forming galaxies can be a powerful tool in understanding their formation and evolution, because the clustering strength provides information about the dark matter halos these galaxies reside in. The descendants (and progenitors) of these galaxies can then be traced by analysing the evolution of the halos themselves. Despite our relatively small sample size, we note that it is selected in a relatively narrow redshift range with little dilution of the projected clustering, so we attempt to estimate the clustering strength of Hα emitters using the angular correlation function, $\omega(\theta)$, from which we can derive the physical correla-
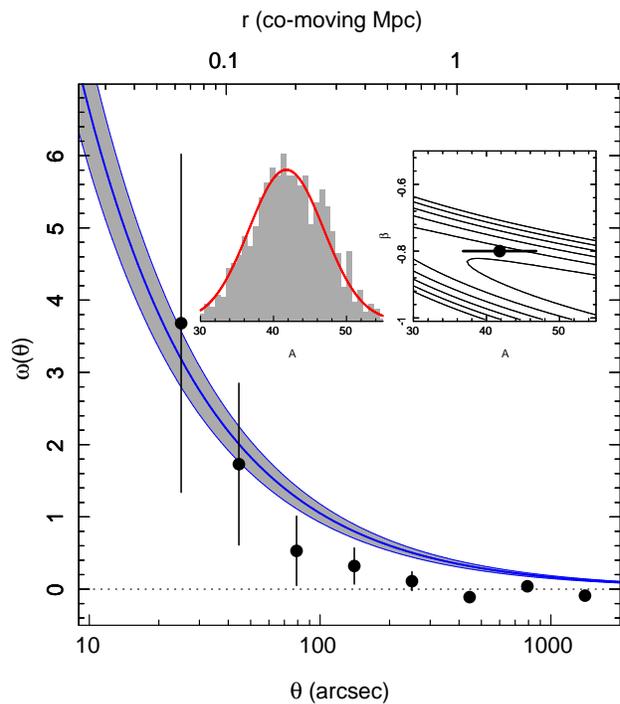
Figure 9. The two-point angular correlation function of Hα emitters, $\omega(\theta)$. The data are fit with a power law $A\theta^{-0.8}$, and we find $A = 41.8 \pm 5.0$ (for θ in arcseconds), corresponding to a correlation length $r_0 = 4.2^{+0.4}_{-0.2}\,h^{-1}$ Mpc. The insets show the likely uncertainty on the fit. The histogram shows the distribution of amplitudes when $\omega(\theta)$ is recalculated for a different realisation of the random catalogue (this was repeated 1000 times). The contour plot represents χ^2 when the fit is allowed to vary both the amplitude and slope β of the power-law fit, thus demonstrating the covariance dependence on the uncertainty in A. We find an adequate fit is obtained without varying β, and therefore in our estimates we fix it at the fiducial value of $\beta = -0.8$, but it appears a better fit would be found for $\beta \sim -1$, and a larger amplitude. The effect of this increase in amplitude and β would correspond to a slight decrease in r_0: $A = 95$, $\beta = -1$ corresponds to $r_0 \sim 3.6\,h^{-1}$ Mpc; in better agreement with the measurement from the simulation (§4.3.2). Thus our current estimate of the clustering strength might be a slight overestimate. These are preliminary findings – a better estimate requires a larger sample. However, these initial results suggest moderate clustering on scales of 10–100″ (i.e. sub-Mpc or sub-halo).

tion length, r_0. We use the estimator proposed by Landy & Szalay (1993):

$$\omega(\theta) = 1 + \left(\frac{N_R}{N_D}\right)^2 \frac{DD(\theta)}{RR(\theta)} - 2\frac{N_R}{N_D}\frac{DR(\theta)}{RR(\theta)}. \quad (4)$$

Here $DD(\theta)$ is the number of pairs of real 'data' galaxies within $(\theta, \theta + \delta\theta)$, $DR(\theta)$ is the number of data-random pairs and $RR(\theta)$ is the number of random-random pairs. N_R and N_D are the number of random and data galaxies in the survey. The random catalogue is generated by uniformly distributing $20N_D$ false galaxies over a geometry corresponding to the survey field-of-view, which is appropriate for the small sample. The errors for each angular interval (spaced at 0.25 dex) are estimated with $\delta\omega(\theta) = (1 + \omega(\theta))/\sqrt{DD(\theta)}$, which estimates the Poisson noise in each bin (Landy & Szalay 1993). We present our results in Figure 9, and fit the data with a power-law of the form $A\theta^{-0.8}$, where A is the amplitude of the angular correlation function, and the power-law index -0.8 is the fiducial value. For θ in arcseconds, we find

$A = 41.8 \pm 5.0$. The uncertainty is the 1σ range of A when the fit is repeated for 1000 realisations of $\omega(\theta)$, with different random catalogues. The integral constraint, C, which accounts for bias introduced by only observing a small region of the sky, will result in a reduction of the amplitude of the two point correlation function: $A(\theta^{-0.8} - C)$. We estimate the effect following Roche et al. (2002), and find it to be small for our survey area, with $C = 0.0055$ for θ in arcseconds – we include it when fitting the amplitude A.

A more useful description of the physical clustering of galaxies is the real-space correlation length, r_0, and this can be calculated directly from the angular correlation function using the inverse Limber transformation (Peebles 1980; Efstathiou et al. 1991) which relates the spatial correlation function to the angular correlation function (provided the redshift distribution is known).

Using clustering simulations described below, we have modeled the effect of the Gaussian filter selection function on our clustering measurements. We compare the projected clustering amplitude, A, derived for the population in a uniformly selected volume (i.e. assuming a top-hat transmission function) to that derived for samples selected with a luminosity-dependent selection function appropriate for our filter transmission curve. We find no statistical difference when including a luminosity-dependent volume correction, with $\langle A_{\mathrm{Gaussian}} \rangle \simeq \langle A_{\mathrm{uniform}} \rangle \sim 45$, using 100 simulations for each method. Therefore, for simplicity in the following deprojection analysis we treat the projected correlation amplitude as if it came from a uniformly selected sample over the narrow redshift slice at $z = 2.22$–2.25. We also assume that the real space correlation function is independent of redshift over this narrow range (this is the same approach used in other high redshift narrow-band surveys, e.g. Kovač et al. 2007).

We find $r_0 = 4.2^{+0.4}_{-0.2} \, h^{-1}$ Mpc, where the uncertainty is derived by reevaluating r_0 after applying the 1-σ uncertainty on the fit to $\omega(\theta)$ described above. This likely underestimates the true error due to added effects such as cosmic variance, which the reader should note could be an important effect in our 220×10^3 Mpc^3 survey and to assess this we now turn to our simulations.

4.3.2 Comparison to theoretical predictions of the clustering properties of star-forming galaxies

In addition to the luminosity distribution predicted by semi-analytic recipes (§4.2.2), we can also compare observed clustering properties of Hα emitters to theoretical predictions from these same models. The B06 model populates dark matter halos within a ΛCDM framework cosmology, where the 'observable' properties such as optical luminosity are dictated by a physically motivated prescription for the behaviour of baryons cooling within the halos. Thus, we can directly evaluate r_0 for Hα emitters within the simulation volume.

Taking the B06 model, we limit simulated luminosities to the range $42 \leqslant \log L_{\mathrm{H}\alpha} \, (\mathrm{erg \, s^{-1}}) \leqslant 44$ (approximately the range of observed luminosities) and $W_{\mathrm{H}\alpha} > 50$Å, and then project the positions of the galaxies onto a 2D 'sky'. We then measure the amplitude of the two-point angular correlation function and convert to r_0 in exactly the same way as before (§4.3.1). We find $r_0 = 5.7^{+0.6}_{-0.7} \, h^{-1}$ Mpc, slightly larger than our observed value (but within $\sim 2\sigma$). Part of this disparity could be due to the slight excess of bright Hα emitters in the simulations: the clustering of Hα emitters in the $z = 0.24$ study of Shioya et al. (2008) was seen to increase with $L_{\mathrm{H}\alpha}$. The reader should also take into account the relatively small size of our survey (despite it being the largest to date) compared to the effective area of the Milli-Millennium. Thus, there
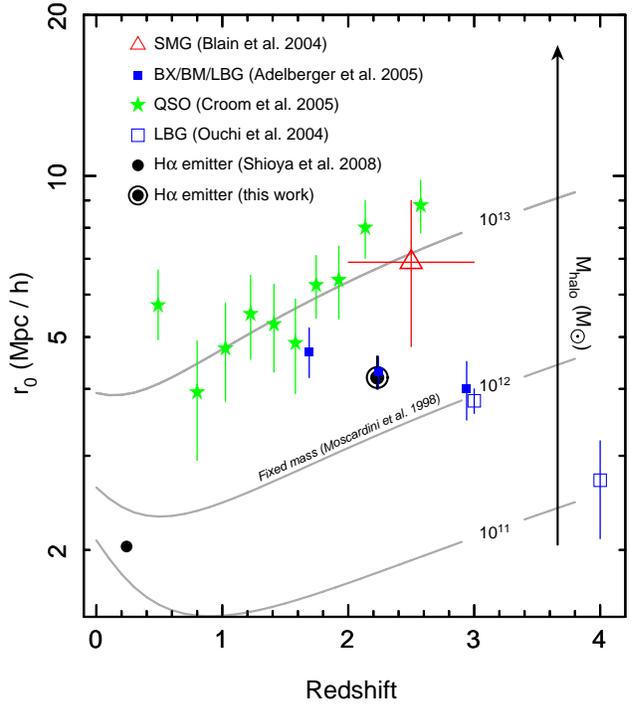
Figure 10. Evolution of the correlation length r_0 in co-moving Mpc for a variety of galaxy populations over $z = 0$–4. Literature points include submm galaxies (Blain et al. 2004); QSOs (Croom et al. 2005); LBGs (Ouich et al. 2004; 2005); BM/BX galaxies (Adelberger et al. 2005), and local Hα selected galaxies (Shioya et al. 2008). We relate the clustering properties to the expected clustering from models of the clustering of dark matter halos, assuming a model for the evolution of bias (Moscardini et al. 1998). Our results suggest that Hα emitters at $z = 2.23$ are hosted by dark matter halos of mass $\sim 10^{12} \, M_\odot$ – in good agreement with the masses of halos expected to host similarly selected galaxies at the same redshift (i.e. BM/BX galaxies). Thus, these Hα emitters appear to be the progenitors of Milky Way-like galaxies at $z = 0$.

are additional uncertainties on our estimate of r_0 due to the likely field-to-field variations which are still significant on this scale.

One way of illustrating this is to randomly select sub-volumes in the Milli-Millennium box corresponding to our survey volume. Projecting galaxies selected in these sub-volumes allows us to evaluate the amplitude of their angular correlation function in an identical way to that performed in §4.3.1. The scatter in amplitude (fixing the power-law slope to the fiducial value, -0.8, as before) for a set of random positions is a good indicator of the expected Cosmic variance on these scales. Statistically we find a similar amplitude to the real data, $\langle A \rangle \sim 45 \pm 31$ (for θ in arcseconds), but with large scatter from the field-to-field variations. Thus, the dominant source of uncertainty in our measurement of the clustering strength of these objects is Cosmic variance, exacerbated by the relatively small numbers of objects in our sample.

4.3.3 Halo mass

The bias parameter describes how the observed galaxy distribution traces the underlying matter distribution. Assuming a model for the evolution of bias over cosmic time, it is possible to estimate the host halo mass of different galaxy populations by comparing their correlation length, r_0 to that of galaxies within halos of various mass.

More importantly, this analysis can provide clues to determine the progenitor populations of galaxy populations in the local Universe. In Figure 10, we compare our results to predictions of $r_0(z)$ for dark matter halos with a fixed *minimum* mass dark matter halos of mass $M_{\rm min} > 10^{11-13} \, h^{-1} \, M_\odot$ (Matarrese et al. 1997; Moscardini et al. 1998). This has become a popular way to present the results of clustering analyses in a cosmological context (e.g. Overzier et al. 2003; Blain et al. 2004; Farrah et al. 2006). We assume a ΛCDM cosmology, and an evolving bias model $b(z)$ (Moscardini et al. 1998). We use the values tabulated by Moscardini et al. (1998) for various fixed minimum mass halos. We evaluate the predicted r_0 of galaxies by solving $\xi_{\rm gal}(z) = D(z)^2 b(z)^2 \xi_{\rm DM}(0)$, where $D(z)$ is the growth factor and ξ is the real space correlation function.

Our results suggest that Hα emitters at $z = 2.23$ reside in moderate mass halos, with $M_{\rm min}$ of order $10^{12} \, M_\odot$, similar to that of a Milky Way mass halo at $z = 0$, suggesting that these high redshift star-forming galaxies are the progenitors of $M_\star$ galaxies seen today. Given that the semi-analytic model is tied directly to the underlying dark matter halos it is possible to extract the halo masses that the B06 Hα emitters actually reside in. Limiting the model luminosities to the observed range, we find halo masses spanning $\log M_{\rm halo} \, (M_\odot) = 11.2 - 12.9$. with a median of $\log M_{\rm halo} \, (M_\odot) = 11.7$. This is in reasonable agreement with the halo mass estimate from the observed deprojected angular correlation function.

In comparison to other active populations at the same epoch (QSOs, SMGs and UV-selected BX/BM galaxies), we see that Hα emitters typically reside in lower-mass halos than SMGs and QSOs and are not directly related to them, but the Hα emitters have a similar clustering strength to BX/BMs at the same redshift (Fig 10). This is perhaps not surprising, given the overlap in selection between the two populations (Fig. 3), and suggests moderate clustering of star-forming galaxies at this redshift.

5 SUMMARY

We have presented results from the largest near-infrared narrow-band survey for Hα emission at $z = 2.23$ yet undertaken, probing 220×10^3 co-moving Mpc^3 to a Hα line flux of $1 \times 10^{-16} \, \mathrm{erg \, s^{-1} \, cm^{-2}}$. Selecting potential $z = 2.23$ Hα emitters on the basis of the significance of their narrow-band excess at $2.121 \mu m$ and broad-band colours and magnitudes, we detect 55 galaxies over 0.603 square degrees in the COSMOS field, a volume density of $(2.5 \pm 0.3) \times 10^{-4} \, \mathrm{Mpc}^{-3}$. Our findings can be summarised as follows:

• The luminosity function is well fit by a Schechter function with $\phi^\star = (1.45 \pm 0.47) \times 10^{-3} \, \mathrm{Mpc}^{-3}$, $\log L^\star = 42.83 \pm 0.13 \, \mathrm{erg \, s^{-1}}$ assuming a faint end slope of $\alpha = -1.35$, as found by Gallego et al. (1995) for the Hα LF at $z = 0$. We find strong evolution in the Hα luminosity function from $z = 0$–2.23 equivalent to a $10\times$ increase in characteristic luminosity. The $z = 2.23$ LF is very similar to the $z = 1.3$ distribution of Yan et al. (1999), implying little evolution in the population between these epochs. We note however that deeper observations will be required to probe the faint end of the LF, which could impact on our estimate of the integrated $\rho_{\rm SFR}$.

• The extinction corrected SFRD determined from the integrated LF is $0.17^{+0.16}_{-0.09} \, M_\odot \, \mathrm{yr}^{-1} \, \mathrm{Mpc}^{-3}$ for $L_{\rm H\alpha} > 10^{42} \, \mathrm{erg \, s}^{-1}$ $z = 2.23$ (including a 15% correction for AGN contamination to the luminosity density). This result for the first time directly traces

the evolution of $\rho_{\rm SFR}$ out to $z = 2.23$ using Hα alone, and supports the view that the SFRD undergoes a plateau at $z \sim 1$–2 prior to sharp decline to the present day.

• The Hα emitters have infrared and radio properties similar to that expected for local star-forming galaxies: our statistical measurement as of the $24 \mu m$ and $21 \, cm$ flux densities are consistent with a LIRG SED at $z = 2.23$, with the infrared derived SFR agreeing with the Hα derived rate if we assume the canonical Hα extinction, $A_{\rm H\alpha} = 1 \, mag$. However, in comparison to M 82 (an archetypal LIRG), we observe a UV light excess over the template, which suggests that these galaxies are not as obscured as M 82, or at least the escape efficiency of UV photons is higher in these galaxies. *HST*-ACS imaging reveals that the Hα emitters have a range of morphologies including compact and disturbed systems: several comprise of two components separated on scales of $\lesssim 10''$ kpc, indicating recent or ongoing merger activity, as might be expected for starburst galaxies. Quantitatively the rest-frame UV-morphologies of the Hα emitters are similar to UV-selected star-forming ('BX') galaxies at the same redshift, with mean half-light radii of $r_{1/2} = 2.1 \pm 0.5 \, kpc$.

• We have performed the first clustering analysis of Hα emitters at $z = 2.23$. First, we measure the amplitude of the two-point angular correlation function $\omega(\theta)$, and find $A = 41.8 \pm 5.0$ for θ in arcseconds. The inverse Limber transform provides us with the real-space correlation length r_0, which we find is $r_0 = 4.2^{+0.4}_{-0.2} \, h^{-1} \, \mathrm{Mpc}$. Comparing this result to other galaxy populations over cosmic time, these high redshift star forming galaxies have similar clustering properties to similarly selected galaxies at high and low redshift, and reside in dark matter halos of masses of $\sim 10^{12} \, M_\odot$. This is agrees with the range of masses of host halos of Hα emitters selected from the Millennium simulation. Our Hα emitters appear to be slightly less strongly clustered than QSOs and SMGs, but similar to BX/BM galaxies at this redshift. Comparisons to models of clustering evolution taking into account bias evolution, our results suggest that these galaxies will likely evolve into $L^\star$ galaxies, similar to the Milky Way at $z = 0$.

These observations represent the first results of an innovative survey for emission line objects over several square degrees at $z = 0.84$, 1.47 and 2.23 corresponding to narrow-bands in J, H and K: the Hi-Z Emission Line Survey (HiZELS) on UKIRT. The outcome of this survey will be large samples (~ 1000 at each redshift) of identically selected 'typical' star-forming galaxies within well defined volumes. The large area will enable us to place even stronger constraints on the star formation history over this crucial epoch from identically selected star-forming galaxies in each redshift slice. Our custom-made J and H narrow-band filters at $1.204 \mu m$ and $1.618 \mu m$ respectively will not only detect Hα emission at $z = 0.84$ and $z = 1.47$, but also [O II]$\lambda 3727$ and [O III]$\lambda 5007$ emission lines from sources at $z = 2.23$, exactly the same redshift as the current $2.121 \mu m$ survey. This will be a useful test for confirming the redshifts of a subset $z = 2.23$ Hα emitters by matching to detections in these other narrow-band filters. It will also provide a more complete survey of the emission line population of star-forming galaxies and AGN at this epoch.

REFERENCES

Adelberger, K. L., Steidel, C. C., Shapley, A. E., Hunt, M. P., Erb, D. K., Reddy, N. A., Pettini, M., 2004, ApJ, 607, 226

Adelberger, K. L., Steidel, C. C., Pettini, M., Shapley, A. E., Reddy, N. A., Erb, D. K., 2005, ApJ, 619, 697

Afonso, J., Cram, L., Mobasher, B., 2000, ApJ, 536, 68

Aragón-Salamanca, A., Alonso-Herrero, A., Gallego, J., García-Dabó, C. E., Pérez-González, P. G., Zamorano, J., Gil de Paz, A., 2003, Astronomical Society of the Pacific Conference Series, Eds.: Perez, E., Gonzalez Delgado, R. M., Tenorio-Tagle, G., 297, 191

Avni, Y., Soltan, A., Tananbaum, H., Zamorani, G., 1980, ApJ, 238, 800

Beckwith, S. V. W., Thompson, D., Mannucci, F., Djorgovski, S. G., 1998, ApJ, 504, 107

Bertin, E. and Arnouts, S., 1996, A&AS, 117, 393

Blain, A. W., Chapman, S. C., Smail, I., Ivison, R., 2004, ApJ, 611, 725

Bolzonella, M., Miralles, J.-M., Pelló, R., 2000, A&A, 363, 476

Borys, C., Smail, I., Chapman, S. C., Blain, A. W., Alexander, D. M., Ivison, R. J., 2005, ApJ, 635, 853

Bower, R. G., Benson, A. J., Malbon, R.,Helly, J. C., Frenk, C. S., Baugh, C. M., Cole, S., Lacey, C. G., 2006, MNRAS, 370, 645 (B06)

Boyle, B. J., Terlevich, R. J., 1998, MNRAS, 293 L49

Boyle, B. J., Shanks, T., Croom, S. M., Smith, R. J., Miller, L., Loaring, N., Heymans, C., 2000, MNRAS, 317, 1014

Boyle, B. J., Cornwell, T. J., Middelberg, E., Norris, R. P., Appleton, P. N., Smail, I., 2007, MNRAS, 376, 1182

Bruzual A., G., Charlot, S. 1993, ApJ, 405, 538

Bunker, A. J., Warren, S. J., Hewett, P. C., Clements, D. L., 1995, MNRAS, 273, 513

Capak, P. et al., 2007, ApJS, 172, 99

Casali, M. et al., B., 2007, A&A, 467, 777

Chapman, S. C., Blain, A. W., Smail, I., Ivison, R. J., 2005, ApJ, 622, 772

Cole, S., Lacey, C. G., Baugh, C. M., Frenk, C. S., 2000, MNRAS, 319, 168

Cox, A. N., Allen's astrophysical quantities, 4th ed. Publisher: New York: AIP Press; Springer, 2000. Edited by Arthur N. Cox. ISBN: 0387987460

Croom, S. M., et al., 2005, MNRAS, 356, 415

Cutri, R. M. et al., 2003, 2MASS All Sky Catalogue of point sources, The IRSA 2MASS All-Sky Point Source Catalogue, NASA/IPAC Infrared Science Archive. http://irsa.ipac.caltech.edu/applications/Gator/

Daddi, E., Cimatti, A., Renzini, A., Fontana, A., Mignoli, M., Pozzetti, L., Tozzi, P., Zamorani, G., 2004, ApJ, 617, 746

Dye, S. et al, 2006, MNRAS, 372, 1227

Erb, D. K., Steidel, C. C., Shapley, A. E., Pettini, M., Adelberger, K. L., 2004, ApJ, 612, 122

Erb, D. K., Steidel, C. C., Shapley, A. E., Pettini, M., Reddy, N. A., Adelberger, K. L., 2006, ApJ, 646, 107

Efstathiou, G., Bernstein, G, Tyson, J. A., Katz, N., Guhathakurta, P., 1991, ApJ, 380, L47

Farrah, D., et al., 2006, ApJ, 641, L17

Förster-Schreiber, N. et al., 2006, ApJ, 645, 1062

Fujita, S. S., Ajiki, M., Shioya, Y., Nagao, T., Murayama, T., Taniguchi, Y., Umeda, K., Yamada, S., Yagi, M., Okamura, S., Komiyama, Y., 2003, ApJ, 586, L115

Gallego, J., Zamorano, J., Aragon-Salamanca, A., Rego, M., 1995, ApJ, 455, L1

Glazebrook, K., Blake, C., Economou, F., Lilly, S., Colless, M., 1999, MNRAS, 306, 843

Hao, L., et al., 2005, AJ, 129, 1795

Hopkins, A. M., Connolly, A. J., Haarsma, D. B., Cram, L. E., 2001, AJ, 122, 288

Ibar, E. et al., 2008, MNRAS, in press

Jansen, R. A., Franx, M., Fabricant, D., 2001, ApJ, 551, 825

John, T. L., 1988, A&A, 193, 189

Hopkins, A. M., 2004, ApJ, 615, 209

Kennicutt, Jr., R. C., Kent, S. M., 1983, AJ, 88, 1094

Kennicutt, Jr., R. C., 1992, ApJ, 388, 310

Kennicutt, Jr., R. C., 1998, ARA&A, 36, 189

Kovač, K., Somerville, R. S., Rhoads, J. E., Malhotra, S., Wang, J., 2007, ApJ, 668, 15

Kurk, J. D., Pentericci, L., Overzier, R. A., Röttgering, H. J. A., Miley, G. K., 2004, A&A, 428, 817

Landy, S. D. and Szalay, A. S., 1993, ApJ, 412, 64

Law, D. R., et al., 2007, ApJ, 656, 1

Le Delliou, M., Lacey, C., Baugh, C. M., Guiderdoni, B., Bacon, R., Courtois, H., Sousbie, T., Morris, S. L., 2005, 357, L11

Leitherer, C., Schaerer, D., Goldader, J. D., Delgado, R. M. G., Robert, C., Kune, D. F., de Mello, D. F., Devost, D., Heckman, T. M., 1999, ApJS, 123, 3

Lilly, S. J., Tresse, L., Hammer, F., Crampton, D., Le Fevre, O., 1995, ApJ, 455, 108

Lilly, S. .J., et al., 2007, ApJS, 172, 70

Madau, P., Ferguson, H. C., Dickinson, M. E., Giavalisco, M., Steidel, C. C., Fruchter, A., 1996, MNRAS, 283, 1388

Matarrese, S., Coles, P., Lucchin, F., Moscardini, L., 1997, MNRAS, 286, 115

Miller, G. E., Scalo, J. M., 1979, ApJS, 41, 513

Mobasher, B. et al., 2007, ApJS, 172, 117

Moorwood, A. F. M., van der Werf, P. P., Cuby, J. G., Oliva, E., 2000, A&A, 326, 9

Moorwood, A., van der Werf, P., Cuby, J. G., Oliva, T., 2003, Rotation, Masses of Galaxies at $z \sim 3.2$, The Mass of Galaxies at Low, High Redshift, 302, Eds.: Bender, R., Renzini, A.

Moscardini, L., Coles, P., Lucchin, F., Matarrese, S., 1997, MNRAS, 299, 95

Ouchi M., et al., 2004, ApJ, 611, 685

Overzier, R. A., Röttgering, H. J. A., Rengelink, R. B., Wilman, R. J., 2003, A&A, 405, 53

Pascual, S. et al., 24, 268

Peebles, P. J. E., 1980, The large-scale structure of the universe, Princeton University Press

Reddy, N. A., et al., 2008, ApJ, 175, 48.

Roche, N. D., Almaini, O, Dunlop, J., Ivison, R. J., Willott, C. J., 2002, MNRAS, 337, 1282

Sanders, D. B. et al., 2006, First Results from S-COSMOS: the Spitzer Legacy Survey of the HST-ACS 2sq.deg. Field, Bulletin of the American Astronomical Society, 38, 1211

Sawicki, M., 2002, AJ, 124, 3050

Schinnerer, E. et al., 2007, ApJS, 172, 46

Scoville, N. et al., 2007, ApJS, 172, 1

Shaver, P. A., Wall, J. V., Kellermann, K. I., Jackson, C. A., Hawkins, M. R. S., 1996, Nature, 384, 439

Shioya, Y., et al., 2007, astro-ph/0709.1009

Smail, I., Ivison, R. J., Blain, A. W., Kneib, J.-P., 2002, MNRAS, 331, 495

Springel V., et al., 2005, Nature, 435, 629

Steidel, C. C., Giavalisco, M., Pettini, M., Dickinson, M., Adelberger, K. L., 1996, ApJ, 462, L17

Steidel, C. C., Adelberger, K. L., Shapley, A. E., Pettini, M., Dickinson, M., Giavalisco, M., 2003, ApJ, 592, 728

Teplitz, H. I., Malkan, M., McLean, I. S., 1998, ApJ, 506, 519

Thompson, D., Mannucci, F., Beckwith, S. V. W., 1996, AJ, 112, 1794

Tresse, L., Maddox, S. J., Le Fèvre, O., Cuby, J.-G., 2002, MNRAS, 337, 369

van der Werf, P. P., Moorwood, A. F. M., Bremer, M. N., 2000, A&A, 362, 509

Villar, V., et al., 2008, ApJ, 677, 169

Yan, L., McCarthy, P. J., Freudling, W., Teplitz, H. I., Malumuth, E. M., Weymann, R. J., Malkan, M. A., 1999, ApJ, 519, L47